

# Augmentations to the Noah Model Physics for Application to the Yellow River Source Area. Part II: Turbulent Heat Fluxes and Soil Heat Transport

DONGHAI ZHENG

*Faculty of Geo-Information Science and Earth Observation, and Faculty of Engineering Technology,  
University of Twente, Enschede, Netherlands*

ROGIER VAN DER VELDE AND ZHONGBO SU

*Faculty of Geo-Information Science and Earth Observation, University of Twente, Enschede, Netherlands*

XIN WANG AND JUN WEN

*Key Laboratory of Land Surface Process and Climate Change in Cold and Arid Regions, Cold and Arid Regions  
Environmental and Engineering Research Institute, Chinese Academy of Sciences, Lanzhou, China*

MARTIJN J. BOOIJ AND ARJEN Y. HOEKSTRA

*Faculty of Engineering Technology, University of Twente, Enschede, Netherlands*

YINGYING CHEN

*Institute of Tibetan Plateau Research, Chinese Academy of Sciences, Beijing, China*

(Manuscript received 9 October 2014, in final form 31 March 2015)

## ABSTRACT

This is the second part of a study on the assessment of the Noah land surface model (LSM) in simulating surface water and energy budgets in the high-elevation source region of the Yellow River. Here, there is a focus on turbulent heat fluxes and heat transport through the soil column during the monsoon season, whereas the first part of this study deals with the soil water flow. Four augmentations are studied for mitigating the overestimation of turbulent heat flux and underestimation of soil temperature measurements: 1) the muting effect of vegetation on the thermal heat conductivity  $\kappa_h$  is removed from the transport of heat from the first to the second soil layer, 2) the exponential decay factor  $\beta_{\text{veg}}$  imposed on  $\kappa_h$  is calculated using the ratio of the leaf area index (LAI) over the green vegetation fraction (GVF), 3) Zilitinkevich's empirical coefficient  $C_{\text{ztl}}$  for turbulent heat transport is computed as a function of the momentum roughness length  $z_{0,m}$ , and 4) the impact of organic matter is considered in the parameterization of the thermal heat properties. Although usage of organic matter for calculating  $\kappa_h$  improves the correspondence between the estimates and laboratory measurements of heat conductivities, it is shown to have a relatively small impact on the Noah LSM performance even for large organic matter contents. In contrast, the removal of the muting effect of vegetation on  $\kappa_h$  and the parameterization of  $\beta_{\text{veg}}$  greatly enhances the soil temperature profile simulations, whereas turbulent heat flux and surface temperature computations mostly benefit from the modified  $C_{\text{ztl}}$  formulation. Further, the nighttime surface temperature overestimation is resolved from a coupled land–atmosphere perspective.

## 1. Introduction

Exchanges of energy and mass at the land–atmosphere interface play an important role in weather and climate

dynamics. Climatic studies have demonstrated that an accurate quantification of these exchanges by atmospheric general circulation models (AGCMs) is crucial to arrive at the bottom boundary states needed for a reliable weather forecast across various time scales (e.g., Beljaars and Holtslag 1991; Koster et al. 2004; Seneviratne et al. 2006). The soil temperature directly affects the exchange of energy near the land surface as the upward longwave

---

*Corresponding author address:* Donghai Zheng, University of Twente, P.O. Box 217, 7500 AE Enschede, Netherlands.  
E-mail: d.zheng@utwente.nl

radiation and sensible and ground heat fluxes depend on it (e.g., Godfrey and Stensrud 2008; Mahanama et al. 2008). Although significant progress has been made by the land surface community to improve the modeling of surface heat fluxes and soil temperature (e.g., Koster et al. 2006; Niu et al. 2011; Sellers et al. 1997), there is still a great challenge to find ways to further reduce uncertainties and strive for consistency between model results and observations (Decker et al. 2012; Dirmeyer et al. 2006; Jiménez et al. 2011; Xia et al. 2013).

Land–atmosphere exchanges on the Tibetan Plateau exert a profound impact on the atmospheric circulation in the Northern Hemisphere and specifically the evolution of the Asian monsoon (Sato and Kimura 2007; Wu and Zhang 1998; Zhou et al. 2009). For this reason, various field campaigns have been conducted in the past [e.g., Global Energy and Water Cycle Experiment (GEWEX) Asian Monsoon Experiment–Tibet (GAME-Tibet; Koike et al. 1999) and Coordinated Enhanced Observing Period (CEOP) Asia–Australia Monsoon Project in Tibet (CAMP-Tibet; Koike 2004)] and monitoring programs are ongoing [e.g., Tibetan Observation and Research Platform (TORP); Ma et al. 2008]. Moreover, several regional-scale soil moisture and soil temperature monitoring networks have been developed recently (Su et al. 2011; Yang et al. 2013). All these activities will undoubtedly continue to contribute to advance our understanding of the prevailing hydrometeorological processes in this high-altitude alpine region, also known as the Third Pole Environment (Ma et al. 2009; Yang et al. 2009, 2014). Improvement in modeling energy transport through the soil column as well as between the land and atmosphere is one of the outstanding issues, which can be resolved via analyses of existing and forthcoming datasets. For instance, previous studies have found that 1) the daytime land surface temperature  $T_{\text{sfc}}$  and sensible heat flux  $H$  are under- and overestimated by model simulations, respectively (e.g., Chen et al. 2011; Zheng et al. 2014); 2) the nighttime  $T_{\text{sfc}}$  simulation is unrealistic under stable atmospheric stratification conditions (e.g., Zeng et al. 2012); and 3) the simulated heat transfer through the soil column is too weak to be able to reproduce the temperature variability measured in the deep soil, and the partitioning of  $H$  and the latent heat flux (LE) is biased (van der Velde et al. 2009).

A possible solution from these previous studies for amelioration of the daytime  $T_{\text{sfc}}$  and  $H$  simulations is to improve the parameterization of the diurnally varying roughness length for heat transport  $z_{0,h}$ , which has notably little impact on the nighttime  $T_{\text{sfc}}$  simulation. Zeng et al. (2012) suggested improving the nighttime  $T_{\text{sfc}}$  simulation by constraining the ground heat flux  $G_0$  as the

sensible and ground heat fluxes are complementary over bare soil, but one can question its validity for vegetation sites. Van der Velde et al. (2009) showed that the simulation of turbulent heat fluxes and soil heat flow can be improved by making a distinction between the soil thermal properties of the upper and deep soil layers and by calibrating the soil and vegetation parameters. However, they arrived at unrealistically high values for the volumetric quartz fraction for the soil matrix to increase the heat conductance through the soil column. This is inconsistent with the findings of Yang et al. (2005) that the existence of dense vegetation roots and abundance of organic matter in the topsoil may significantly reduce thermal conductivity. Although Chen et al. (2012) have started to investigate the stratification of soil thermal properties induced by organic matter, the effects of the vertical heterogeneity on simulating heat fluxes and soil temperature profiles remain unknown.

This paper is the second part of a study that has been set up to improve the state-of-the-art Noah land surface model (LSM) in its ability to simultaneously reproduce soil moisture and temperature profiles measured in the high-elevation source region of the Yellow River (SRYP) on the Tibetan Plateau. The emphasis of the first part lies on the model physics associated with the soil water flow, while this part focuses on the soil heat transport and turbulent heat flux processes. A comprehensive dataset that includes in situ micrometeorological and soil moisture–temperature profile measurements, as well as soil properties characterized in the laboratory, is utilized here to assess the suitability of default model parameterizations and model augmentations.

This paper is outlined as follows. Section 2 introduces the Noah model physics defining the surface energy balance and soil heat flow simulations. Section 3 describes the augmentations made to the Noah model structure aimed at improving the turbulent and soil heat transport processes. Section 4 presents the comparison of laboratory soil thermal property measurements with estimates computed using the newly developed parameterization that accommodates the effect of organic matter. Section 5 reports on the performance of Noah in simulating turbulent heat fluxes and soil temperature in its default configuration as well as with augmentations. Section 6 provides a discussion on the simulation of nighttime  $T_{\text{sfc}}$ , presents Noah simulations whereby both soil moisture and heat flow processes are considered dynamically, and reports on the model performance in a case when adopting very high organic matter contents. Finally, in section 7 conclusions are drawn. A detailed description of the study area and the in situ and laboratory measurements utilized for this investigation is available in Zheng et al. (2015, hereafter Part I).

## 2. Noah LSM

The Noah, version 3.4.1, model physics associated with surface energy balance and soil heat flow are given below. Detailed descriptions of the soil water transport and root water uptake processes can be found in [Part I](#). Unless stated otherwise, a modified version of the default model is utilized here that is capable of ingesting the measured upward shortwave radiation and soil moisture to avoid those uncertainties that affect the performance in simulating the turbulent heat fluxes and soil heat transport as in [Zheng et al. \(2014\)](#).

### a. Surface energy balance

The surface energy balance equation solved by the Noah LSM can be written as

$$S^\downarrow - S^\uparrow + \varepsilon(L^\downarrow - \sigma T_{\text{sfc}}^4) = H + \text{LE} + G_0, \quad (1)$$

where  $S^\downarrow$  ( $S^\uparrow$ ) is the downward (upward) shortwave radiation ( $\text{W m}^{-2}$ ),  $L^\downarrow$  is the downward longwave radiation ( $\text{W m}^{-2}$ ),  $T_{\text{sfc}}$  is the ground surface temperature (K),  $\varepsilon$  is the surface emissivity (unitless), and  $\sigma$  is the Stefan–Boltzmann constant (taken as  $5.67 \times 10^{-8} \text{W m}^{-2} \text{K}^{-4}$ ). Variables  $H$  ( $\text{W m}^{-2}$ ),  $\text{LE}$  ( $\text{W m}^{-2}$ ), and  $G_0$  ( $\text{W m}^{-2}$ ) are as previously defined.

The sensible heat flux is described with bulk equations based on the Monin–Obukhov similarity theory (MOST; i.e., [Chen et al. 1997](#)):

$$H = \rho c_p C_h u (\theta_{\text{sfc}} - \theta_a) \quad \text{and} \quad (2a)$$

$$C_h = \frac{k^2/R}{\left[ \ln\left(\frac{z}{z_{0,m}}\right) - \Psi_m\left(\frac{z}{L}\right) + \Psi_m\left(\frac{z_{0,m}}{L}\right) \right] \left[ \ln\left(\frac{z}{z_{0,h}}\right) - \Psi_h\left(\frac{z}{L}\right) + \Psi_h\left(\frac{z_{0,h}}{L}\right) \right]}, \quad (2b)$$

where  $\rho$  is the density of air ( $\text{kg m}^{-3}$ );  $c_p$  is the specific heat of air ( $\text{J kg}^{-1} \text{K}^{-1}$ );  $C_h$  is the surface exchange coefficient for heat transfer (unitless);  $u$  is the mean wind speed ( $\text{m s}^{-1}$ );  $\theta_{\text{sfc}}$  is the potential temperature at the surface (K);  $\theta_a$  is the potential air temperature (K);  $k$  is the von Kármán constant (taken as 0.4);  $R$  is related to the turbulent Prandtl number ( $\text{Pr}$ ) and taken as 1.0;  $z$  is the observation height (m);  $z_{0,m}$  is the roughness length for momentum transfer (m);  $z_{0,h}$  (m) is as previously defined;  $L$  is the Obukhov length (m); and  $\Psi_m$  and  $\Psi_h$  are the stability correction functions for momentum and sensible heat transfer (unitless), respectively, which are derived from [Paulson \(1970\)](#) as given in the [appendix](#).

The potential evapotranspiration  $\text{LE}_p$  is calculated diurnally using a Penman-based approach ([Chen et al. 1996](#); [Mahrt and Ek 1984](#)):

$$\text{LE}_p = \frac{\Delta(R_n - G_0) + \rho \lambda C_h u (q_s - q)}{1 + \Delta} \quad \text{and} \quad (3a)$$

$$R_n = S^\downarrow - S^\uparrow + \varepsilon(L^\downarrow - \sigma T_{\text{sfc}}^4), \quad (3b)$$

where  $\Delta$  is the slope of the relation between the saturated vapor pressure and the temperature ( $\text{kPa K}^{-1}$ ),  $R_n$  is the net radiation ( $\text{W m}^{-2}$ ),  $\lambda$  is the latent heat of vaporization ( $\text{J kg}^{-1}$ ), and  $q_s$  ( $q$ ) is the saturated (actual) specific humidity ( $\text{kg kg}^{-1}$ ). Note that herein the surface exchange coefficient for heat transfer is assumed to be equivalent to that of water vapor transport. The estimation of actual evapotranspiration ( $\text{LE}$ ) is performed by applying a Jarvis-type surface resistance

scheme to impose soil and atmospheric constraints ([Chen et al. 1996](#)).

The ground surface heat flux is calculated following Fourier's law using the temperature gradient between the surface and the midpoint of the first soil layer:

$$G_0 = \kappa_{h,0} \frac{T_{\text{sfc}} - T_{s,1}}{\Delta z_1}, \quad (4)$$

where  $\kappa_{h,0}$  is the thermal heat conductivity of the surface layer ( $\text{W m}^{-1} \text{K}^{-1}$ ),  $T_{s,1}$  is the temperature of the first soil layer (K), and  $\Delta z_1$  is the depth between the surface and the midpoint of the first soil layer (m).

For the estimation of the ground surface temperature, the following linearization based on a first-order Taylor series expansion is utilized ([van der Velde et al. 2009](#)):

$$T_{\text{sfc}}^4 \approx T_a^4 \left[ 1 + 4 \left( \frac{T_{\text{sfc}} - T_a}{T_a} \right) \right]. \quad (5)$$

Substitution of [Eq. \(5\)](#) into the surface energy balance equation [[Eq. \(1\)](#)] yields the following expression for the ground surface temperature:

$$T_{\text{sfc}} = T_a + \frac{S^\downarrow - S^\uparrow + \varepsilon L^\downarrow - H - \text{LE} - G_0}{4\varepsilon\sigma T_a^3} - \frac{1}{4} T_a, \quad (6)$$

where  $T_a$  is the air temperature (K). Readers are referred to [Ek and Mahrt \(1991\)](#) for detailed information on the numerical implementation of the surface energy balance equations [[Eqs. \(1\)–\(6\)](#)].

### b. Soil heat flow

The transport of heat through the soil column is governed by the thermal diffusion equation:

$$C_s \frac{\partial T}{\partial t} = \frac{\partial}{\partial z} \left( \kappa_h \frac{\partial T}{\partial z} \right), \quad (7)$$

where  $\kappa_h$  is the thermal heat conductivity ( $\text{W m}^{-1} \text{K}^{-1}$ ) and  $C_s$  is the thermal heat capacity ( $\text{J m}^{-3} \text{K}^{-1}$ ).

The solution to Eq. (7) is achieved using the fully implicit Crank–Nicholson scheme. The temperature at the bottom boundary is defined as the annual mean surface air temperature, which is specified here as 275 K at a depth of 8 m based on observations collected at the Maqu station. The top boundary is confined by the ground surface temperature.

### c. Soil thermal parameterization

The heat flow through the soil column is parameterized by  $\kappa_h$  and  $C_s$ , which depend on all constituents of the soil matrix. The thermal heat capacity is calculated using the following equation:

$$C_s = \theta C_w + (1 - \theta_s) C_{\text{soil}} + (\theta_s - \theta) C_{\text{air}}, \quad (8)$$

where  $\theta$  is the soil moisture content ( $\text{m}^3 \text{m}^{-3}$ );  $\theta_s$  is the porosity ( $\text{m}^3 \text{m}^{-3}$ ); and  $C$  represents the heat capacity ( $\text{J m}^{-3} \text{K}^{-1}$ ) with subscripts  $w$ ,  $\text{soil}$ , and  $\text{air}$  referring to water, solid soil, and air. In the Noah LSM,  $C_w$ ,  $C_{\text{soil}}$ , and  $C_{\text{air}}$  are taken as  $4.2 \times 10^6$ ,  $2.0 \times 10^6$ , and  $1005 \text{ J m}^{-3} \text{K}^{-1}$ , respectively.

The thermal heat conductivity is calculated as a combination of the saturated  $\kappa_{\text{sat}}$  and dry  $\kappa_{\text{dry}}$  thermal heat conductivity weighted proportionally to the degree of saturation (Johansen 1975):

$$\kappa_h(\theta) = K_e (\kappa_{\text{sat}} - \kappa_{\text{dry}}) + \kappa_{\text{dry}}, \quad (9a)$$

where  $K_e$  is the Kersten (1949) number representing the degree of saturation and is defined by

$$K_e = \begin{cases} \log_{10}(\theta/\theta_s) + 1.0, & \text{for } \theta/\theta_s > 0.1 \\ 0.0, & \text{for } \theta/\theta_s \leq 0.1 \end{cases}. \quad (9b)$$

The dry thermal heat conductivity is calculated using a semiempirical equation:

$$\kappa_{\text{dry}} = \frac{0.135 \rho_b + 64.7}{2700 - 0.947 \rho_b} \quad \text{and} \quad (9c)$$

$$\rho_b = (1 - \theta_s) 2700, \quad (9d)$$

where  $\rho_b$  is the bulk density of dry soil ( $\text{kg m}^{-3}$ ).

The saturated thermal heat conductivity is calculated as the geometric mean of the heat conductivities of the materials present within the soil matrix:

$$\kappa_{\text{sat}} = \kappa_{\text{soil}}^{1-\theta_s} \kappa_w^{\theta_s}, \quad (9e)$$

where  $\kappa_w$  is the heat conductivity of water (taken as  $0.57 \text{ W m}^{-1} \text{K}^{-1}$ ) and  $\kappa_{\text{soil}}$  is the heat conductivity of solid soil that is estimated as a function of the volumetric quartz fraction (qtz):

$$\kappa_{\text{soil}} = \kappa_{\text{qtz}}^{\text{qtz}} \kappa_o^{1-\text{qtz}}, \quad (9f)$$

where  $\kappa_{\text{qtz}}$  and  $\kappa_o$  are the heat conductivities of quartz and other soil particles, which are taken as 7.7 and  $2.0 \text{ W m}^{-1} \text{K}^{-1}$ , respectively. The volumetric quartz fraction is taken equivalent to the fraction sand (Peters-Lidard et al. 1998).

The Noah LSM has a single heat source model structure, that is, the vegetation and soil surface are represented by a single layer. Because the two media have clearly different thermal properties and dynamics,  $\kappa_{h,0}$  is the conductivity defining the heat transport from the surface to the midpoint of the upper soil layer reduced as a function of the green canopy according to

$$\kappa_{h,0} = \kappa_h(\theta_1) \exp(-\beta_{\text{veg}} \text{GVF}), \quad (10)$$

where GVF is the green vegetation fraction (unitless),  $\beta_{\text{veg}}$  is the constant muting factor taken as 2.0, and  $\theta_1$  is the soil moisture content of the first soil layer ( $\text{m}^3 \text{m}^{-3}$ ).

Exponential decay of the green canopy is also imposed on the heat conductivity of the first soil layer  $\kappa_{h,1}$  by Noah, while the heat conductivities of other soil layers only depend on the constituents of the soil matrix, which are calculated as follows:

$$\kappa_{h,i} = \begin{cases} \kappa_h(\theta_i) \exp(-\beta_{\text{veg}} \text{GVF}), & \text{for } i = 1 \\ \kappa_h(\theta_i), & \text{for } i > 1 \end{cases}, \quad (11)$$

where  $i$  is the soil layer,  $\kappa_{h,i}$  is the heat conductivity of each soil layer adopted by Eq. (7), and  $\kappa_h(\theta_i)$  is calculated using Eqs. (9a)–(9f).

### d. Roughness length parameterization

The surface exchange coefficient for heat [Eq. (2b)] is of importance for a reliable calculation of the  $H$  [Eq. (2a)] and  $\text{LE}_p$  [Eq. (3a)], which depends on parameterization of roughness lengths for momentum and heat transfer. The roughness length for momentum transport is calculated in Noah, version 3.4.1, as a function of the time-varying GVF:

$$z_{0,m} = (1 - \text{GVF}_{\text{norm}}) z_{0,m_{\text{min}}} + \text{GVF}_{\text{norm}} z_{0,m_{\text{max}}} \quad \text{and} \quad (12a)$$

$$\text{GVF}_{\text{norm}} = \frac{\text{GVF} - \text{GVF}_{\text{min}}}{\text{GVF}_{\text{max}} - \text{GVF}_{\text{min}}}, \quad (12b)$$

where  $z_{0,m_{\min}}$  and  $z_{0,m_{\max}}$  are prescribed based on vegetation type and are selected for this investigation as in Zheng et al. (2014). Further, GVF is deduced from the 10 daily synthesis normalized difference vegetation index (NDVI) product from the Système Pour l'Observation de la Terre (SPOT) as previously described in Zheng et al. (2014) and Chen et al. (2013).

The Reynolds number ( $Re_*$ )-dependent formulation of the  $kB^{-1}$  [ $= \ln(z_{0,m}/z_{0,h})$ ] concept proposed by Zilitinkevich (1995) is utilized to calculate the thermal roughness length (Chen et al. 1997) as follows:

$$z_{0,h} = z_{0,m} \exp(-\kappa C_{zil} \sqrt{Re_*}) \quad \text{and} \quad (13a)$$

$$Re_* = u_* z_{0,m} / \nu, \quad (13b)$$

where  $k$  is as previously defined,  $B$  is the Stanton number,  $u_*$  is the friction velocity ( $\text{m s}^{-1}$ ),  $\nu$  is the kinematic molecular viscosity (taken as  $1.5 \times 10^{-5} \text{m}^2 \text{s}^{-1}$ ), and  $C_{zil}$  is an empirical constant specified as 0.1 analogously to values derived from measurements over grassland (Chen et al. 1997).

### 3. Augmentations to the Noah LSM

#### a. Vegetation effect on heat transport through soil

Recently, van der Velde et al. (2009), Rosero et al. (2010), and Niu et al. (2011) have reported on the underestimation of the heat conductance through the soil column using the Noah LSM for vegetation areas. Rosero et al. (2010) pointed out that the value for  $\beta_{\text{veg}}$  may be too high, which unrealistically reduces the values for  $\kappa_{h,0}$  and  $\kappa_{h,1}$  as well as the simulation of  $G_0$  and the heat transport from or toward the second soil layer. The  $G_0$  calculations can be improved by lowering the  $\beta_{\text{veg}}$  from 2.0 to 1.0 for grassland as Rosero et al. (2010) suggested, but this does not resolve the poor heat conductance toward the deep soil. In fact, the impact of vegetation on the heat conductance from the first to second soil layer is questionable. We suggest, therefore, to parameterize  $\kappa_{h,0}$  and  $\kappa_{h,1}$  independent from each other, whereby the exponential decay of  $\kappa_h$  as a function of the GVF is only imposed on  $\kappa_{h,0}$  as given in Eq. (10) whereas it is ignored for  $\kappa_{h,1}$  by changing Eq. (11) as

$$\kappa_{h,i} = \kappa_h(\theta_i). \quad (14)$$

The investigation by Rosero et al. (2010) indicates that a lower value for  $\beta_{\text{veg}}$  is needed. Other LSMs reduce the surface heat flux, instead of the heat conductivity, as a function of the vegetation cover. Early versions of the Variable Infiltration Capacity model (VIC; Liang et al. 1999; Peters-Lidard et al. 1997) adopted, for instance,

$$G_0 = G_{0,\text{bs}} \exp(-0.5\text{LAI}), \quad (15)$$

where  $G_{0,\text{bs}}$  is the surface heat flux under bare soil ( $\text{W m}^{-2}$ ) and LAI is the leaf area index ( $\text{m}^2 \text{m}^{-2}$ ). From this, we can derive the following expression for  $\beta_{\text{veg}}$  through combination with Eqs. (4) and (10):

$$\beta_{\text{veg}} \approx \begin{cases} 0.5\text{LAI}/\text{GVF}, & \text{for } \text{GVF} > 0 \\ 0, & \text{for } \text{GVF} = 0 \end{cases}. \quad (16)$$

Here, GVF and LAI are derived from the 10-daily synthesis SPOT NDVI product analogously to the roughness length parameterization as given in Zheng et al. (2014) and Chen et al. (2013).

#### b. $C_{zil}$ parameterization

The surface exchange coefficient for heat is another source of uncertainty that can be responsible for the overestimation of the sensible heat flux and underestimation of surface temperature during daytime by the Noah LSM as has been reported in Chen et al. (2011), Niu et al. (2011), and Zeng et al. (2012). The most practical approach toward resolving this issue without violating the integrity of the model structure is through improvement of the  $kB^{-1}$  parameterization.

Both Zeng et al. (2012) and Zheng et al. (2014) recognized that this can be accomplished through a better quantification of the empirical  $C_{zil}$  parameter. Zheng et al. (2014) evaluated all  $kB^{-1}$  parameterizations developed for the Noah LSM and found that the best performance was achieved with the formulation proposed by Chen and Zhang (2009), which can be expressed by

$$C_{zil} = 10^{-0.4h}, \quad (17a)$$

where  $h$  is the canopy height (m). This expression is implemented as an option in Noah, version 3.4.1, but has not yet been taken up in the default model despite promising results. Further, it should be noted that within Noah, version 3.4.1, the canopy height is related to the  $z_{0,m}$  by assuming that  $z_{0,m}$  is 7% of the canopy height (Mölder and Lindroth 1999), which can be expressed as

$$h = z_{0,m}/0.07. \quad (17b)$$

#### c. Organic matter effect on soil thermal parameterization

As described in section 2c, both the soil heat capacity and conductivity depend on all constituents of the soil matrix and, thus, on organic matter as well. In the default configuration, the Noah LSM does not accommodate the effect of organic matter on the soil thermal properties. However, Eq. (8) can be modified fairly

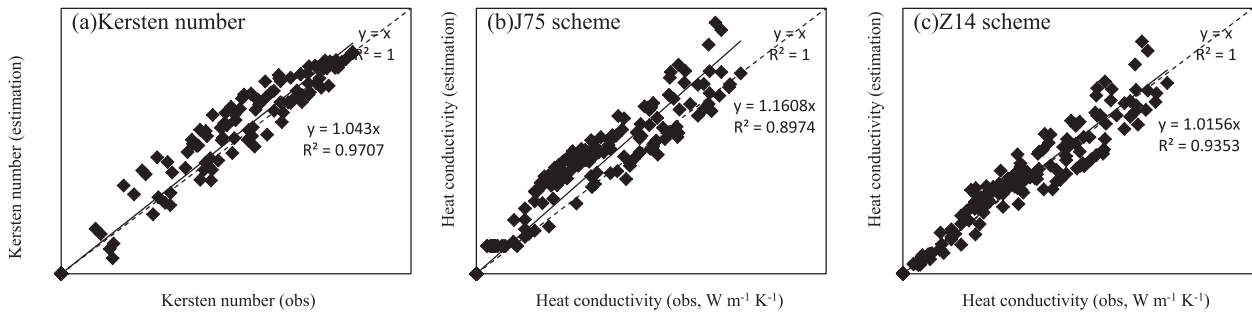


FIG. 1. Scatterplots of laboratory-measured and computed (a) Kersten number, (b)  $\kappa_h$  with Eqs. (9a)–(9f), and (c)  $\kappa_h$  with Eqs. (19a) and (19b) of soil samples collected around SRYR in July 2013.

easily to include the volumetric fraction of solid organic content  $f_{s,\text{soc}}$  according to the concept proposed by de Vries (1963) as follows:

$$C_s = \theta C_w + (\theta_s - \theta) C_{\text{air}} + (1 - \theta_s) f_{s,\text{soc}} C_{\text{soc}} + (1 - \theta_s)(1 - f_{s,\text{soc}}) C_{\text{min}} \quad \text{and} \quad (18a)$$

$$f_{s,\text{soc}} = \frac{m_{\text{soc}} \rho_{s,\text{min}}}{m_{\text{soc}} \rho_{s,\text{min}} + (1 - m_{\text{soc}}) \rho_{s,\text{soc}}}, \quad (18b)$$

where  $C_{\text{soc}}$  is the heat capacity of soil organic content (taken as  $2.5 \times 10^6 \text{ J m}^{-3} \text{ K}^{-1}$ ),  $C_{\text{min}}$  is the heat capacity of the mineral soil fraction (taken as  $2.0 \times 10^6 \text{ J m}^{-3} \text{ K}^{-1}$ ),  $m_{\text{soc}}$  is the mass fraction of the soil organic content ( $\text{kg kg}^{-1}$ ),  $\rho_{s,\text{min}}$  is the particle density of the mineral soil fraction (taken as  $2700 \text{ kg m}^{-3}$ ), and  $\rho_{s,\text{soc}}$  is the particle density of the soil organic content (taken as  $1300 \text{ kg m}^{-3}$ ). It should be noted that the definition [Eq. (18b)] of the fraction of soil organic content is different for the calculation of the thermal properties compared to the one used for the computation of the hydraulic properties.

Further, Johansen (1975) pointed out that the bulk density of a dry soil is a major factor in defining the soil heat conductivity of a dry soil, while the soil texture has little effect on the conductivity. In other words, the semiempirical equation [Eq. (9c)] can be directly utilized to estimate  $\kappa_{\text{dry}}$ , but the formulation for the bulk density of dry soil [Eq. (9d)] needs to be modified to account for the impact of organic matter on the bulk density as described in Part I:

$$\rho_b = \frac{\rho_{b,\text{min}} \rho_{b,\text{soc}}}{m_{\text{soc}} \rho_{b,\text{min}} + (1 - m_{\text{soc}}) \rho_{b,\text{soc}}}, \quad (19a)$$

where  $\rho_{b,\text{min}}$  ( $\rho_{b,\text{soc}}$ ) is the bulk density ( $\text{kg m}^{-3}$ ) of the mineral soil fraction (soil organic content).

On the other hand, Johansen (1975) found that for saturated conditions the bulk density has little impact on the heat conductivity, whereas differences in soil composition become increasingly important for the magnitude of the

conductivity. We accommodate the effect of organic matter on  $\kappa_{\text{sat}}$  via  $\kappa_{\text{soil}}$  by modifying its parameterization as follows:

$$\kappa_{\text{soil}} = \kappa_{\text{soc}} \kappa_{\text{qtz}}^{f_{s,\text{soc}}} \kappa_o^{(1-f_{s,\text{soc}})(1-f_{s,\text{soc}})}, \quad (19b)$$

where  $\kappa_{\text{soc}}$  is the heat conductivity of soil organic content taken as  $0.25 \text{ W m}^{-1} \text{ K}^{-1}$  from Lawrence and Slater (2008).

The effect of soil organic content on  $\kappa_h$  is taken directly into consideration in the computations [Eqs. (9a), (9b)] once the  $\kappa_{\text{dry}}$  and  $\kappa_{\text{sat}}$  are estimated using the updated bulk density and  $\kappa_{\text{soil}}$  formulations, respectively. It should, however, be noted that the Noah-simulated soil thermal properties are also affected by the soil organic content via its impact on the hydraulic properties that regulate the soil moisture dynamics as well as the porosity. The latter is discussed in Part I.

#### 4. Estimation of soil heat conductivity

In this section, the performance of Noah's default  $\kappa_h$  parameterization [Eqs. (9a)–(9f)] and the modified formulation [Eqs. (19a), (19b)] that takes soil organic content into account is evaluated using the laboratory-measured soil properties of samples collected at the high-elevation SRYR. Soil samples were collected in July 2013 at two sites near the Maqu micrometeorological station with relatively low organic content in the top soil layer (<3%; see Table 2 in Part I), as well as two sites located in a wetland environment with abundant organic content (>15% near the surface). Detailed descriptions of the soil sampling and laboratory measurements can be found in Part I.

Figure 1 shows the calculated  $K_e$  and  $\kappa_h$  against values derived from laboratory measurements of all the soil samples using the KD2 Thermal Properties Analyzer (Decagon Devices Inc.). The measured  $K_e$  is derived through inversion of Eq. (9a) using the heat

TABLE 1. Values of  $R^2$ , ME, and RMSE between measured and estimated  $\kappa_{\text{dry}}$ ,  $\kappa_{\text{sat}}$ , and  $\kappa_h$  for samples around Maqu station.

Scheme	$\kappa_{\text{dry}}$			$\kappa_{\text{sat}}$			$\kappa_h$	
	$R^2$	ME ( $\text{W m}^{-1} \text{K}^{-1}$ )	RMSE ( $\text{W m}^{-1} \text{K}^{-1}$ )	$R^2$	ME ( $\text{W m}^{-1} \text{K}^{-1}$ )	RMSE ( $\text{W m}^{-1} \text{K}^{-1}$ )	ME ( $\text{W m}^{-1} \text{K}^{-1}$ )	RMSE ( $\text{W m}^{-1} \text{K}^{-1}$ )
Eqs. (9a)–(9f)	0.362	0.072	0.083	0.729	0.157	0.209	0.144	0.197
Eqs. (19a) and (19b)	0.727	−0.009	0.026	0.811	0.008	0.128	0.022	0.115

conductivities measured over the complete soil moisture range from dry to fully saturated, which provides values of  $\kappa_h$ ,  $\kappa_{\text{dry}}$ , and  $\kappa_{\text{sat}}$ . Figure 1a shows a plot with the measured  $K_e$  versus estimates computed with Eq. (9b). Both the slope of the fitted linear function (close to unity, i.e., 1.043) and the low scatter among data points (coefficient of determination  $R^2 = 0.879$ ) indicate that the  $K_e$  calculations match the measurements fairly well. This confirms that the  $K_e$  concept is also suitable for the soils encountered at the high-elevation SRYR.

Figures 1b and 1c present further comparisons of the  $\kappa_h$  measurements with estimates obtained via Eqs. (9a)–(9f) and Eqs. (19a) and (19b), respectively, of which the latter accommodate the effect of soil organic content. A clear difference is noted in the ability of Eqs. (9a)–(9f) and Eqs. (19a) and (19b) to reproduce the  $\kappa_h$  measurements. The slope of the linear function fitted through Eqs. (19a) and (19b) is closer to unity than that for Eqs. (9a)–(9f) (e.g., 1.015 vs 1.160) and the scatter among the data points in Eqs. (19a) and (19b) is also less, leading to an  $R^2$  of 0.885 versus 0.790. Apparently, soil organic content is responsible for part of the  $\kappa_h$  variability, and its consideration is needed to further optimize the performance of parameterizations.

Table 1 provides the error statistics computed between the measured heat conductivities (e.g.,  $\kappa_h$ ,  $\kappa_{\text{dry}}$ , and  $\kappa_{\text{sat}}$ ) and those estimated with Eqs. (9a)–(9f) and Eqs. (19a) and (19b), such as  $R^2$ , mean error (ME), and root-mean-square error (RMSE). From the error statistics we can deduce that, on average, Eqs. (9a)–(9f) overestimate  $\kappa_{\text{dry}}$  by  $0.072 \text{ W m}^{-1} \text{ K}^{-1}$  and  $\kappa_{\text{sat}}$  by  $0.157 \text{ W m}^{-1} \text{ K}^{-1}$ , leading to an overestimation of  $\kappa_h$  by  $0.144 \text{ W m}^{-1} \text{ K}^{-1}$ . This overestimation of the  $\kappa_h$  measurements is largely resolved through the consideration of soil organic content by Eqs. (19a) and (19b). However, it should be noted that, apart from the bias, a large part of the random differences between the measured and computed  $\kappa_{\text{dry}}$  is also reduced given the increase of the  $R^2$  from 0.362 to 0.727.

## 5. Noah simulations

### a. Numerical experiments

Five experiments are performed to assess the impact of the augmentations (see section 3) to the default Noah

LSM on the turbulent heat flux and soil temperature profile simulations using measurements collected at Maqu station located in the high-elevation SRYR. The Noah LSM is first run with the default soil property and roughness length parameterization (section 2), which is hereafter called Ctrl. The second experiment (EXP1) contains a Noah model run whereby the muting effect of vegetation on the heat conductivity from the midpoint of the first soil layer toward the midpoint of the second soil layer is removed and a distinction is made between  $\kappa_{h,0}$  and  $\kappa_{h,1}$ . The third experiment (EXP2) consists of a simulation whereby the default value of  $\beta_{\text{veg}}$  in the Noah model structure is replaced by an expression [Eq. (16)] as a function of the LAI and GVF. For the fourth experiment (EXP3), a Noah model run is made with Zilitinkevich's empirical coefficient  $C_{\text{zil}}$  parameterized as an indirect function of canopy height via  $z_{0,m}$  (see section 3b) instead of a constant value. The default soil thermal parameterization is modified to the one that considers the effect of soil organic content for the fifth experiment (EXP4).

An overview of these numerical experiments is provided in Table 2. The Noah model is run for all the experiments over the period from 8 June to 30 September 2010 using measured atmospheric forcing data. Model initialization, selection of the vegetation and soil parameters are identical to the simulations reported in Part I. Readers are referred to either Zheng et al. (2014) or Part I for details on the study area (Maqu station) and the micrometeorological and soil temperature measurements.

### b. Turbulent heat fluxes and soil temperature profiles

Figure 2 shows the mean diurnal variability for June–September of the measured and simulated turbulent (sensible and latent) heat fluxes and soil temperature profiles. Tables 3 and 4 provide the ME and RMSE, respectively, computed between the measured and simulated turbulent heat fluxes and soil temperature profiles. Analysis of the measurements (black dots in Fig. 2) reveals that the latent heat flux is, on average, more than twice as large as the sensible heat flux during daytime. Further, it is noted that the amplitude of the diurnal temperature cycle diminishes with depth as expected and is almost completely vanished at the midpoint on

TABLE 2. List of numerical experiments designed to test augmentations for the Noah LSM.

Expt	$\kappa_{h,0}$ and $\kappa_{h,1}$	$\beta_{veg}$	$C_{zil}$	Heat properties
Ctrl	Same [Eqs. (10), (11)]	Constant (2.0)	Constant (0.1)	Default (section 2c)
EXP1	Different [Eqs. (10), (14)]	Constant	Constant	Default
EXP2	Different	Variable [Eq. (16)]	Constant	Default
EXP3	Different	Variable	Variable [Eqs. (17a), (17b)]	Default
EXP4	Different	Variable	Variable	New (section 3c)

the third soil layer (70 cm). Also, the phase of the diurnal temperature cycle is affected by the soil depth, showing that the maximum temperature is reached at a later time at greater depths.

In its default configuration, Noah (Ctrl) overestimates both the daytime (0900–1800 Local Time) sensible (Fig. 2a)

and latent (Fig. 2b) heat fluxes and somewhat underestimates the heat fluxes after dusk (1900–2400 Local Time). Most notable is the daytime LE overestimation, which can be larger than  $50 \text{ W m}^{-2}$ . On the other hand, the Ctrl model run underestimates the daytime surface temperature (Fig. 2c) because  $H$  and LE affect the

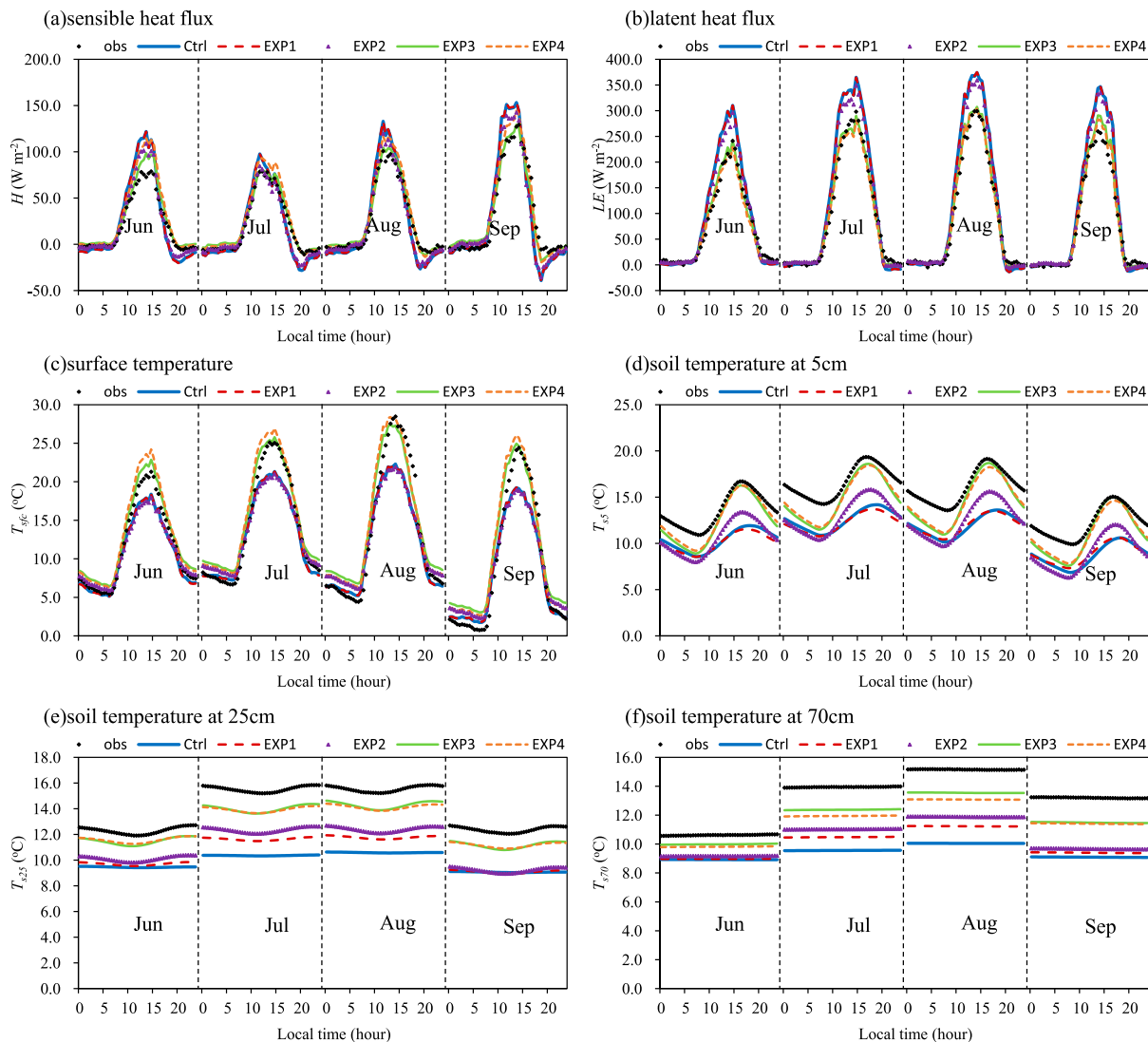


FIG. 2. Average diurnal cycles of June–September measured and simulated (a) sensible heat flux; (b) latent heat flux; (c) surface temperature; and (d)–(f) soil temperatures at 5-, 25-, and 70-cm depth produced by five numerical experiments.

TABLE 3. Values of ME computed between the measured and simulated  $H$ , LE,  $T_{\text{sfc}}$ ,  $T_{s,5}$ ,  $T_{s,25}$ , and  $T_{s,70}$  produced by five numerical experiments.

Expt	ME					
	$H$ ( $\text{W m}^{-2}$ )	LE ( $\text{W m}^{-2}$ )	$T_{\text{sfc}}$ (K)	$T_{s,5}$ (K)	$T_{s,25}$ (K)	$T_{s,70}$ (K)
Ctrl	1.78	27.29	-1.07	-3.77	-4.16	-3.97
EXP1	1.72	27.11	-1.09	-3.84	-3.44	-3.31
EXP2	-0.05	22.93	-0.68	-3.32	-2.96	-2.88
EXP3	3.46	3.51	1.31	-1.43	-1.23	-1.43
EXP4	7.72	-0.42	1.44	-1.37	-1.27	-1.73

TABLE 4. Values of RMSE computed between the measured and simulated  $H$ , LE,  $T_{\text{sfc}}$ ,  $T_{s,5}$ ,  $T_{s,25}$ , and  $T_{s,70}$  produced by five numerical experiments.

Expt	RMSE					
	$H$ ( $\text{W m}^{-2}$ )	LE ( $\text{W m}^{-2}$ )	$T_{\text{sfc}}$ (K)	$T_{s,5}$ (K)	$T_{s,25}$ (K)	$T_{s,70}$ (K)
Ctrl	24.38	54.75	2.85	3.93	4.36	4.19
EXP1	24.71	54.88	2.86	4.01	3.51	3.45
EXP2	20.44	46.86	2.99	3.39	3.01	2.99
EXP3	14.12	30.93	2.48	1.76	1.29	1.50
EXP4	17.44	30.36	2.62	1.61	1.35	1.81

magnitude of the computed surface temperature negatively [see Eq. (6)]. Moreover, an underestimation of the temperatures at soil depths of 5 (Fig. 2d), 25 (Fig. 2e), and 70 cm (Fig. 2f) ( $T_{s,5}$ ,  $T_{s,25}$ , and  $T_{s,70}$ , respectively) is found. This can be explained by the fact that less heat is entering the soil column during daytime because of overestimations of  $H$  and LE, and more heat is released during nighttime because of the heat flux ( $H$  and LE) underestimations.

The turbulent heat fluxes and  $T_{\text{sfc}}$  produced by EXP1 are nearly identical to the Ctrl simulations. This demonstrates that the separation of heat conductivities for the surface and first soil layer has a minor impact on the turbulent heat flux and  $T_{\text{sfc}}$  simulations. In contrast, the deep soil temperature (e.g.,  $T_{s,25}$  and  $T_{s,70}$ ) simulations are improved in EXP1, particularly for the months July and August when the vegetation cover is largest. This is caused by the removal of the muting effect of vegetation on the heat conductivity from the midpoint of the first soil layer toward the midpoint of the second soil layer. As such, more heat is transported into the soil column, which increases the deep soil temperature. The parameterization of  $\beta_{\text{veg}}$  via Eq. (16) included in EXP2 further improves the deep soil temperature simulations and enlarges the simulated diurnal  $T_{s,5}$  variability. Equation (16) generates lower  $\beta_{\text{veg}}$  ( $\approx 1.0$ ) values, resulting in larger  $\kappa_{h,0}$  [Eq. (10)] and  $G_0$  [Eq. (4)]. As more energy is transported into the soil column, less energy remains for the production of the turbulent heat fluxes, leading to improvements of 4.27 and 8.06  $\text{W m}^{-2}$  in the RMSEs computed between measured and simulated  $H$  and LE in EXP2, respectively. It should, however, be noted that the daytime  $T_{\text{sfc}}$  underestimation remains and that in the morning (0000–0800 Local Time) the EXP2 simulations overestimate  $T_{\text{sfc}}$ , while  $T_{s,5}$  is underestimated. The latter is induced by the lower  $\beta_{\text{veg}}$  that enables an accelerated release of heat from the soil column as will be further elaborated in the discussion.

The overestimation of the daytime turbulent heat fluxes is greatly resolved in the EXP3 model run, for which Zilitinkevich's empirical coefficient  $C_{\text{ztl}}$  is

calculated as an indirect function of canopy height via  $z_{0,m}$  (see section 3b). With this augmentation, the Noah LSM uses higher  $C_{\text{ztl}}$  values and thus computes lower  $C_h$  values [e.g., Eqs. (2b), (13a)]. This leads to the production of less turbulent heat [e.g., Eq. (2a) for  $H$  and Eq. (3a) for LE], which consequently causes an increase in the simulated daytime  $T_{\text{sfc}}$ . Most notably, the RMSEs computed between the measured and simulated turbulent heat fluxes improve by 31% and 34% for  $H$  and LE in comparison to the performance of EXP2, respectively. This is, in particular for the LE, achieved by a reduction in the bias from 22.93 to 3.51  $\text{W m}^{-2}$ .

As less energy is consumed by turbulent transport, more heat is available for the warming of the soil column leading to an improved soil temperature profile simulation. Hence, the underestimation of the measured temperature reduces in comparison to EXP2 by 1.89, 1.73, and 1.45 K for soil depths of 5, 25, and 70 cm, respectively. It should, however, be noted that the overestimation of nighttime  $T_{\text{sfc}}$ , first seen in the EXP2 simulation, is further amplified by the augmentation introduced in EXP3.

The performance of EXP4 is comparable to that of EXP3, implying that consideration of organic matter in the soil thermal parameterization (see section 3c) has little impact on the heat flux and soil temperature simulations at the Maqu micrometeorological station. On the other hand, the soil organic content mass fraction is relatively low for this site (<3%; see section 4). The effect of organic matter on the Noah LSM performance will be further investigated in the discussion through a sensitivity analysis.

### c. Assessment via Taylor diagram

Taylor diagrams (Taylor 2001) are further used to assess the model performance in reproducing the diurnal surface heat flux and soil temperature patterns (with a 30-min interval) in terms of phase and amplitude of unbiased matchups for all five experiments. The magnitude of RMSE as error statistics is largely determined

by the bias between two datasets and may therefore provide an ambiguous view on the model performance. Pearson's product-moment correlation coefficient  $R$  is used as a measure of the agreement between the measured and simulated phase. The normalized standard deviation (std dev) is utilized to evaluate the amplitude, which is defined by

$$\text{std dev} = \hat{\sigma}_f = \sigma_f / \sigma_r, \quad \hat{\sigma}_r = 1, \quad (20)$$

where  $\sigma_f$  ( $\sigma_r$ ) is the standard deviation of a test field (i.e., simulation) [reference field (i.e., measurement)].

In Taylor diagrams, the normalized standard deviation is taken as the radius, whereas the Pearson's correlation coefficient is adopted as the angle of a polar plot. Data points showing a perfect fit with the measurements are located on the  $x$  axis at  $R = 1$  and  $\text{std dev} = 1$ . The distance to this point is the RMSE of two unbiased datasets, which is referred to as the centered normalized RMSE ( $\text{RMSE}_c$ ) and can also be calculated as

$$\text{RMSE}_c = \hat{E}' = E' / \sigma_r \quad \text{and} \quad (21a)$$

$$E' = \left\{ \frac{1}{N} \sum_{i=1}^N [(f_i - \bar{f}) - (r_i - \bar{r})]^2 \right\}^{1/2} \\ = (\text{RMSE}^2 - \text{ME}^2)^{1/2}, \quad (21b)$$

where  $E'$  is the centered RMSE and  $\bar{f}$  and  $\bar{r}$  are the mean values of the simulation and measurement, respectively.

Figure 3 shows that in all the experiments the Noah LSM is able to produce a phase that matches the surface heat flux and soil temperature profile measurements reasonably well, as indicated by the  $R$  values varying from about 0.90 to 0.99. In the case of the simulated LE,  $T_{\text{sfc}}$ , and  $T_{s,5}$ , the magnitude of  $R$  remains about the same for all five model runs. On the other hand, differences are noted among the  $R$  values computed between the measurements and simulations of  $H$ ,  $T_{s,25}$ , and  $T_{s,70}$ , whereby a better agreement in the phase is achieved with the augmentations made for EXP3 (and EXP4).

The Ctrl model run exaggerates the amplitude of the diurnal cycle of the turbulent heat fluxes by more than 25% (e.g.,  $\text{std dev} > 1.25$ ), and underestimates the amplitude of diurnal cycle of the surface and soil temperatures by more than 15% (e.g.,  $\text{std dev} < 0.85$ ). The latter underestimation is most severe for the deep soil temperatures ( $T_{s,25}$  and  $T_{s,70}$ ) and is as large as 60%. The augmentation incorporated in EXP1 largely resolves this bias in the deep soil temperatures, but has little impact on Noah's performance in the turbulent heat flux and near-surface temperature ( $T_{\text{sfc}}$  and  $T_{s,5}$ )

simulations. The major improvement in the simulation of the  $T_{s,5}$  variability is obtained with EXP2 when the vegetation effect on the heat transport through the soil is reconsidered, which also reduces somewhat the overestimation of the turbulent heat flux variability.

With std dev values close to 1.0 for both the  $H$  and LE, the most significant enhancement in the performance of simulating the diurnal turbulent heat flux variability is, however, noted once the  $C_{\text{ztl}}$  is parameterized as (indirect) function of canopy height (EXP3). Because less energy is consumed by the turbulent heat transport, the simulated diurnal surface and soil temperature variability increases yielding a better agreement with the measurements, except for  $T_{s,5}$  in which case the diurnal variability is overestimated. In general, the EXP4 model run produces very similar, but slightly worse std dev values in comparison to EXP3. Only the ability of capturing the diurnal  $H$  variability deteriorates quite drastically with more than 10%, which follows most likely from smaller imperfections in the simulation of the  $T_{\text{sfc}}$ .

The distance of the points in the Taylor diagram to the perfect matchup at  $R = 1$  and  $\text{std dev} = 1$  (or  $\text{RMSE}_c$ ) is typically found for EXP3, and comparable results are obtained by EXP4 in terms of LE and  $T_{\text{sfc}}$ . In the  $T_{s,5}$  simulation, however, EXP2 outperforms EXP3 and EXP4. In essence, this confirms the conclusions drawn based on Fig. 2 and the tables with the RMSE and ME as performance indicators. Nevertheless, the favorable result noted for EXP2 in simulating  $T_{s,5}$  is somewhat surprising, which suggests that room is available for further improving the model physics of the soil heat transport, as will be discussed below.

## 6. Discussion

### a. Improvement of nighttime surface temperature simulation

Although the augmentations proposed for the default Noah LSM (see section 3) greatly improved the performance of turbulent heat fluxes and soil heat transport, one of the remaining issues is the overestimation of nighttime  $T_{\text{sfc}}$ . This leads to the underestimation of nighttime  $T_{s,5}$  (see Fig. 2d) and decreasing performance with respect to the Taylor statistics. Zeng et al. (2012) recently investigated a similar issue associated with the simulation of nighttime  $T_{\text{sfc}}$  by the Noah LSM. They suggested that the problem may be resolved by 1) increasing the number of iterations to secure a converged solution for the MOST equations [Eqs. (2a), (2b)] for turbulent heat transport, 2) modifying the stability function in Eq. (2b) for stable atmosphere conditions, and 3) constraining the ground heat flux.

Obs – Observations, 0 – Ctrl, 1 – EXP1, 2 – EXP2, 3 – EXP3, 4 – EXP4

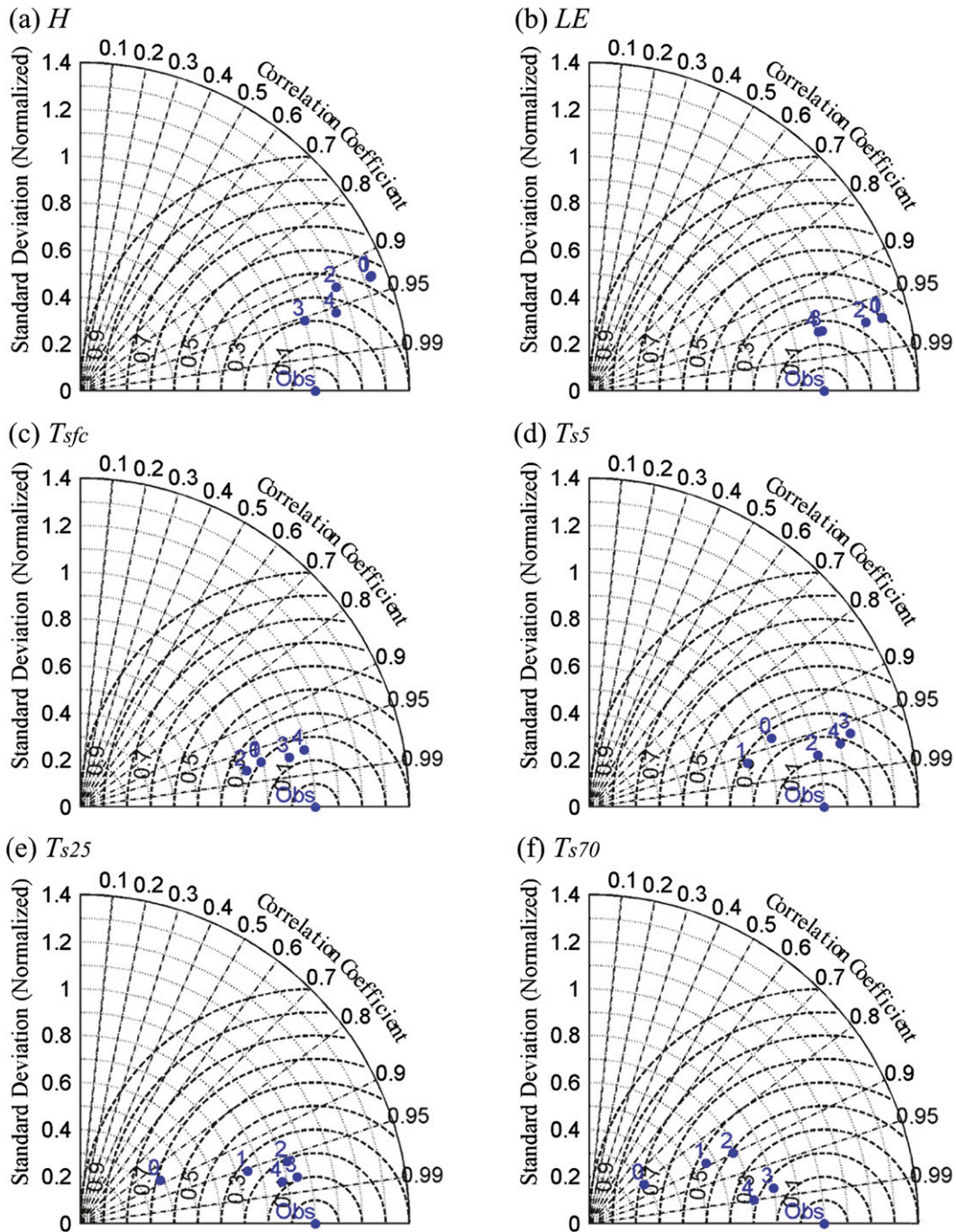


FIG. 3. Taylor diagrams illustrating the model performance as if the measurements and the simulated variables are unbiased: (a) sensible heat flux; (b) latent heat flux; (c) surface temperature; and (d)–(f) soil temperatures at 5-, 25-, and 70-cm depth. The radial distance from the origin is the normalized std dev and the correlation coefficient is displayed as the azimuthal position. Therefore, the distance from the data point to the measurement (located at  $R = 1$  and  $\text{std dev} = 1$ ) is the normalized  $\text{RMSE}_c$ .

TABLE 5. Values of RMSE computed between the measured and simulated  $H$ , LE,  $T_{\text{sfc}}$ ,  $T_{s,5}$ ,  $T_{s,25}$ , and  $T_{s,70}$  produced by the experiments performed for the discussion (section 6).

Expt	RMSE					
	$H$	LE	$T_{\text{sfc}}$ (K)	$T_{s,5}$ (K)	$T_{s,25}$ (K)	$T_{s,70}$ (K)
	( $\text{W m}^{-2}$ )	( $\text{W m}^{-2}$ )				
Ctrl	24.38	54.75	2.85	3.93	4.36	4.19
EXP3	14.12	30.93	2.48	1.76	1.29	1.50
EXPS1	14.12	30.93	2.48	1.76	1.29	1.50
EXPS2a	14.11	30.93	2.48	1.76	1.29	1.50
EXPS2b	14.13	30.93	2.48	1.76	1.29	1.50
EXPS3	14.74	32.39	2.37	1.04	0.84	0.33
EXPS4	19.86	31.45	2.70	1.25	1.01	0.41
EXPS5	20.57	31.50	2.76	1.21	0.96	0.51
EXPS6	29.30	32.00	3.42	1.67	1.21	0.71

In accordance with Zeng et al.'s recommendation, three additional experiments are carried out to investigate the possibility of resolving the nighttime  $T_{\text{sfc}}$  overestimation. First, the maximum number of iterations for the turbulent heat transport is increased from 5 to 30 (hereafter EXP31). Second, the Noah's default stability function for stable conditions by Paulson (1970) is replaced with the formulations proposed either by Holtslag and De Bruin (1988) (hereafter EXPS2a) or by Łobocki (1993) (hereafter EXPS2b). The previously mentioned stability functions are given in the appendix. Third,  $G_0$  is constrained for stable atmospheric conditions by setting  $\beta_{\text{veg}}$  to 2.0 and is hereafter referred to as EXPS3. Other settings of the Noah LSM are kept the same as for EXP3 described in section 5.

Table 5 gives the RMSEs computed between the measured and simulated turbulent heat fluxes and soil temperatures. It indicates that the maximum number of iterations and adopted atmospheric stability function do not affect the model performance as EXPS1, EXPS2a, and EXPS2b yield RMSEs comparable to EXP3. In contrast, the performance in simulating soil temperature profiles ( $T_{s,5}$ ,  $T_{s,25}$ , and  $T_{s,70}$ ) is greatly improved by implementing different  $\beta_{\text{veg}}$  values for stable and unstable conditions (EXPS3). In comparison to EXP3, this reduces the RMSE computed between the measured and simulated soil temperatures for depths of 5, 25, and 70 cm by about 41%, 35%, and 78%, respectively. A decrease in the RMSE is also noted for  $T_{\text{sfc}}$ , while the matchup of measured and simulated turbulent heat fluxes (e.g., LE and  $H$ ) somewhat degrades.

Figure 4 further shows the average diurnal cycle of the measured and simulated turbulent heat fluxes and soil temperatures produced with Ctrl, EXP3, and EXPS3. The overestimation of nighttime  $T_{\text{sfc}}$  invoked by EXP2 and further amplified in EXP3 is considerably mitigated

by the augmentation made for the EXPS3, which leads to the similar improvements in the simulations of deep soil temperature (see Figs. 4d–f). Moreover, amelioration of the nighttime  $T_{\text{sfc}}$  leads also to an enhancement in the nighttime sensible heat flux simulation.

The above results support the suggestion by Zeng et al. (2012) that the issue associated with the heat exchange under stable conditions should be treated from a coupled land–atmosphere rather than from an atmospheric turbulence perspective alone. In other words, deficiencies in simulating nighttime  $T_{\text{sfc}}$  and turbulent heat fluxes can be improved by constraining the  $G_0$  because of the link with the turbulent heat fluxes via the surface energy budget. In the case of EXPS3, a higher value of  $\beta_{\text{veg}}$  (2.0) is utilized to suppress the heat released from the soil column to the surface at night and a lower value of  $\beta_{\text{veg}}$  [ $\approx 1.0$ , computed with Eq. (16)] ensures an accelerated warming of the soil column during the day. Similarly, Best (1998) found that the  $T_{\text{sfc}}$  simulated for a grassland environment does not decrease sufficiently during the night without modifying the role of the vegetation canopy in the surface energy budget calculations.

The rationale for utilizing different daytime and nighttime  $\beta_{\text{veg}}$  values here is associated with the Noah model structure that the soil–vegetation system is represented as a single heat–water vapor source, and the canopy effect on the radiation transfer and surface energy budget computations cannot be explicitly considered. A similar issue was resolved by Wang et al. (2010) through considering the undercanopy resistance, while Niu et al. (2011) substantially revised the Noah LSM to a dual-source model structure. The solution found here by the EXPS3 sensitivity test provides a pragmatic solution to a complex problem without the necessity of changing the Noah model structure. Obviously, a more formal approach with robust physics is preferred and deserves further study.

### b. Impact of soil moisture simulation

Since both thermal heat conductivity and capacity depend on all soil constituents and the soil moisture content (see section 2c), the uncertainties associated with the soil moisture characterizations will affect the soil heat transport simulation. Moreover, the LE produced by the Noah LSM also depends on the water availability in the root zone, and thus, soil moisture affects the computed surface energy budget as well, even though Part I has shown that the available energy is the main driver of LE during the wet monsoon in the study area. Despite the soil moisture profile simulations being greatly improved with the modified soil hydraulic parameterization and vertical root distribution (see Part I),

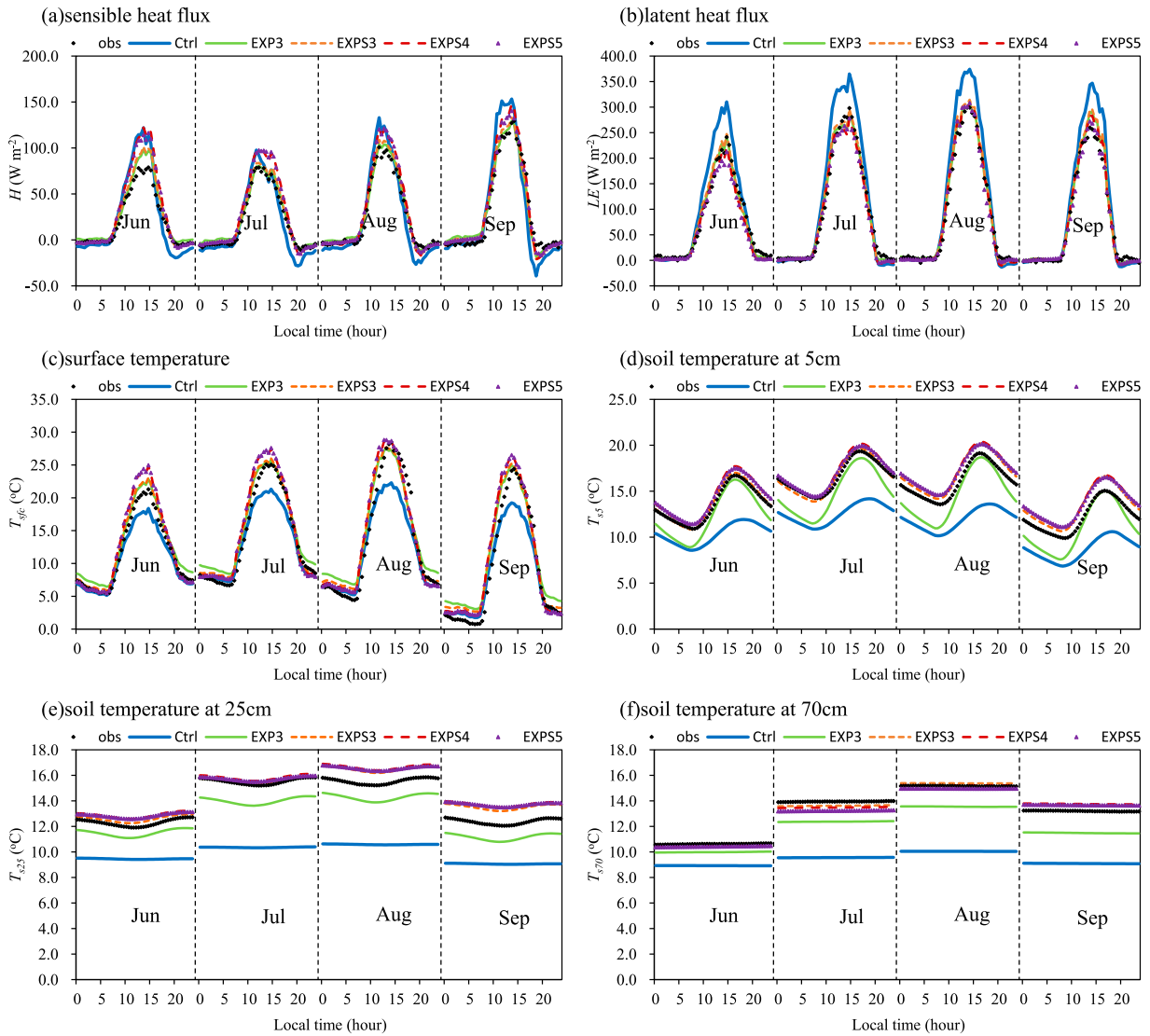


FIG. 4. As in Fig. 2, but for experiments performed for the discussion (section 6).

uncertainties remain with RMSEs of  $0.04$  and  $0.015 \text{ m}^3 \text{ m}^{-3}$  for the surface (e.g., 5 cm) and deeper (e.g., 25 and 70 cm) soil layers, respectively.

Instead of using the measurements, the soil water flow component is invoked (parameterized as EXP2 in Part I) to investigate the impact of soil moisture uncertainties on the turbulent heat flux and soil heat transport simulations, while other settings are as EXPS3 (hereafter EXPS4). The average diurnal cycle of the turbulent heat fluxes and soil temperatures produced by EXPS4 are also plotted in Fig. 4, and Table 5 lists the respective RMSEs. Figure 4 shows that EXPS4 overestimates the daytime  $H$  (Fig. 4a) and  $T_{\text{sf}}c$  (Fig. 4c) with respect to EXPS3 and the measurements, which is likely due to the surface soil moisture underestimation (see Table 6 in

Part I). The soil moisture underestimations in the upper two soil layers (e.g., 5 and 25 cm) also lead to a slight overestimation of temperatures of the corresponding soil layers (see Figs. 4d,e). The EXPS4 RMSEs are about 0.33, 0.21, 0.17, and 0.08 K larger for surface and 5-, 25-, and 70-cm soil temperatures in comparison to EXPS3. Also, the RMSE for  $H$  increases by  $5.12 \text{ W m}^{-2}$ , while the RMSE for  $LE$  improves somewhat ( $0.94 \text{ W m}^{-2}$ ). Nevertheless, the performance of the fully augmented Noah LSM (e.g., EXPS4) performs considerably better than the default Noah LSM that makes use of the soil moisture measurements. This study highlights once again that the surface energy budget calculations by physically based LSMs can only be ameliorated if the water budget is considered as well.

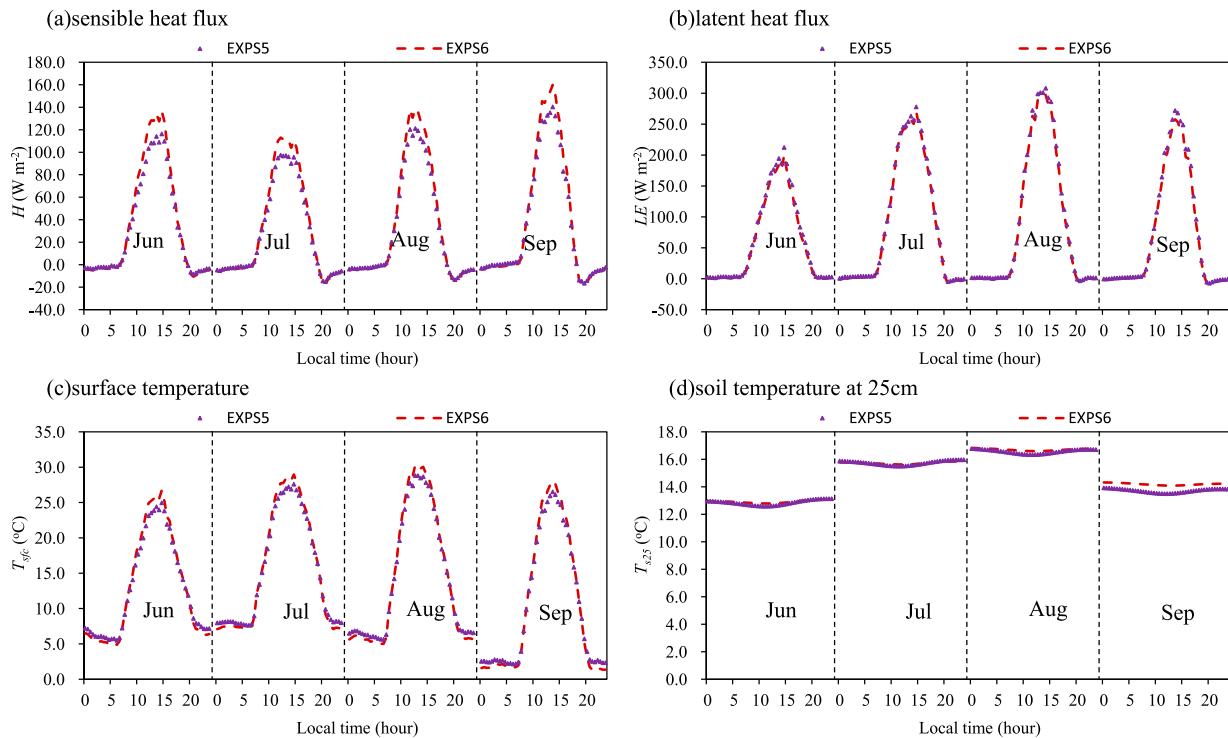


FIG. 5. Average diurnal cycles of June–September simulated (a) sensible heat flux, (b) latent heat flux, (c) surface temperature, and (d) soil temperature at 25-cm depth produced by EXPS5 and EXPS6 to assess the sensitivity for soil organic content (section 6c).

### c. Sensitivity analysis of organic matter parameterization

Although usage of organic matter for calculating the thermal heat conductivity improves the agreement between estimates and laboratory measurements across the entire  $m_{\text{soc}}$  range, the results of section 5 reveal only a small impact on the heat flux and soil temperature simulations for the Maqu micrometeorological station. On the other hand, the Maqu station holds a relatively low  $m_{\text{soc}}$  for the top ( $\sim 2.5\%$ ) as well as the deep soil layers ( $\sim 0.5\%$  at 60 cm), whereas the wetland ecosystems in the region contain a much larger amount of organic matter ( $>15\%$  near the surface). Two additional numerical experiments are carried out to further assess the sensitivity of the model results when  $m_{\text{soc}}$  is considered for both the soil thermal and soil hydraulic parameterizations. For the first experiment (hereafter EXPS5), the consideration of  $m_{\text{soc}}$  is also invoked for the soil thermal parameterization as described in section 3c, while the other settings are taken as in EXPS4. In the second experiment (hereafter EXPS6), Noah is run with the same options as EXPS5 but using  $m_{\text{soc}}$  of the wetland soil profile, for example, 15%, 10%, 5%, and 2.5% for the respective four soil layers.

Figure 5 shows the time series of the average diurnal cycle of the turbulent heat fluxes and soil temperatures produced with EXPS5 and EXPS6. In addition, the average diurnal turbulent heat flux and soil temperature cycle produced by EXPS5 is added to Fig. 4. Further, the RMSEs computed for EXPS5 and EXPS6 are included in Table 5 primarily for reference purposes and not as an accuracy measure, especially for EXPS6. In general, EXPS5 is nearly identical to EXPS4, which confirms the findings of section 5 that consideration of  $m_{\text{soc}}$  in the soil thermal parameterization has little impact on the Noah performance for Maqu station. Similarly, the comparison of the diurnal cycles of EXPS5 and EXPS6 shows that the impact of  $m_{\text{soc}}$  is inferior to the effect of the roughness parameterization. Nevertheless, average differences of about 6 and  $5 \text{ W m}^{-2}$  are noticed for  $H$  and  $LE$ , respectively, and a proportional effect is seen among the simulated temperatures.

## 7. Conclusions

This is Part II of a two-paper series on assessing the Noah land surface model (LSM) performance in simulating surface water and energy budgets in the high-elevation source region of the Yellow River (SRYR).

Here, we investigate the turbulent heat flux and soil heat transport simulated by the Noah LSM through comparisons against sensible ( $H$ ) and latent (LE) heat flux and soil temperature profile measurements taken during the monsoon season (June–September) at the Maqu station. The default Noah LSM constrained by soil moisture profile measurements significantly overestimates the daytime turbulent heat fluxes and underestimates the surface temperature  $T_{\text{sfc}}$ . The soil temperatures are systematically underestimated as well.

Four augmentations to the model physics are investigated for resolving the above deficiencies: 1) the muting effect of vegetation on the soil heat conductivity  $\kappa_h$  from the midpoint of the first soil layer toward the midpoint of the second soil layer is removed, 2) the exponential decay factor  $\beta_{\text{veg}}$  imposed on  $\kappa_h$  is parameterized as a function of the ratio of the leaf area index (LAI) over the green vegetation fraction (GVF), 3) Zilitinkevich's empirical coefficient  $C_{\text{zil}}$  defining the efficiency of turbulent heat transport is parameterized as a function of canopy height via the momentum roughness length  $z_{0,m}$ , and 4) the impact of organic matter is included in the thermal heat conductivity  $\kappa_h$  and capacity  $C_s$  parameterization. The modified soil thermal parameterization is compared against laboratory-measured soil heat conductivities. It is shown that through consideration of organic matter within the default heat conductivity scheme (Johansen 1975) of the Noah LSM, the root-mean-square error (RMSE) computed between the estimated and measured heat conductivities under dry  $\kappa_{\text{dry}}$  and saturated  $\kappa_{\text{sat}}$  soil moisture conditions is reduced by 69% and 39%, respectively. Similar improvements are noted for the estimated heat conductivities at intermediate saturation levels.

Five numerical experiments, including a control run with the default model structure (Ctrl), are designed to progressively assess the impact on the model performance of the four augmentations described above. Removal of the muting effect of vegetation on the soil heat transport from the first layer toward the deep soil increases the diurnal temperature variability simulated for the deep soil by about 50%, while a negligible impact is noted on the turbulent heat flux and  $T_{\text{sfc}}$  simulations. The parameterization of  $\beta_{\text{veg}}$  by the LAI/GVF ratio ( $\approx 1.0$ ) enhances the heat exchange between the land surface and soil column. This mitigates the underestimation of the diurnal temperature variability in the deep soil ( $T_{s,5}$ ,  $T_{s,25}$ , and  $T_{s,70}$ ) and simultaneously alleviates somewhat the turbulent heat flux overestimation. The most significant improvements in the  $T_{\text{sfc}}$  and turbulent heat flux simulations are found once  $C_{\text{zil}}$  is parameterized as a function of the canopy height via  $z_{0,m}$ . However, the model run whereby soil organic

content is used for determining the soil thermal properties does not yield any noticeable improvement with respect to the other numerical experiments performed for Maqu station that hold a relatively low organic matter content  $m_{\text{soc}}$  of 2.5% for the top soil. In comparison to the default model structure, the performance in simulating the turbulent heat fluxes and soil heat transport improves for the Noah LSM with the three most promising augmentations. In this case the RMSEs computed between the measurements and simulations are reduced by about 42%, 44%, 13%, 55%, 70%, and 64% for  $H$ , LE,  $T_{\text{sfc}}$ ,  $T_{s,5}$ ,  $T_{s,25}$ , and  $T_{s,70}$ , respectively.

Three additional experiments are conducted to investigate the remaining issue associated with the overestimation of nighttime  $T_{\text{sfc}}$ . It is found that this problem cannot be solved by considering the atmospheric turbulence alone, but should be treated from a coupled land–atmosphere perspective. Further, the impact of the uncertainty associated with the model's characterization of the soil moisture profile on the simulated surface energy budget is assessed as well. This experiment demonstrates that the fully augmented Noah LSM, including the improved soil water flow (see Part I) as well as the previously described turbulent heat flux and soil heat transport model physics, provides better estimations of turbulent heat fluxes and soil temperatures in comparison to the control run, which is constrained by the soil moisture profile measurements. As such, the performance enhancement achieved with the selected augmentations outweighs the uncertainty introduced by the imperfection in the simulated soil moisture. Furthermore, the impact of  $m_{\text{soc}}$  on the Noah performance is assessed by adopting the case of an organic wetland soil common to the region. This experiment demonstrates that while the consideration of organic matter is imperative for the soil moisture profile, the impact on the heat flux and temperature profile is inferior to other augmentations addressed herein.

This study again highlights that the most effective way to improve the heat flux and soil temperature simulations on the Tibetan Plateau is to improve the parameterization of the diurnally varying roughness length for heat transfer  $z_{0,h}$  as found by previous studies (Chen et al. 2011; Zeng et al. 2012; Zheng et al. 2014). While a significant improvement is achieved in the soil water flow simulation through a better representation of the hydraulic parameterization with the consideration of the organic matter effect (see Part I), it is shown that consideration of organic matter in the soil thermal parameterization has little impact on the heat flux and soil temperature simulations.

Although the Noah LSM simulations are only validated in this study for a site on the Tibetan Plateau, the addressed issues are inherent to the model structure of

the Noah LSM. For instance, the large negative biases in the Noah LSM–simulated soil temperature found by Xia et al. (2013) within the North American Land Data Assimilation System (NLDAS) product may be resolved by adopting the suggested augmentations. An improved simulated near-surface heat exchange provides a more detailed understanding of the land–atmosphere feedbacks and enhances our ability to forecast the impact that climate change might have on the vulnerable high-altitude Tibetan Plateau ecosystems.

*Acknowledgments.* This study was supported by funding from the FP7 CEOP-AEGIS and CORE-CLIMAX projects funded by the European Commission through the FP7

program, the Chinese Academy of Sciences Fellowship for Young International Scientists (Grant 2012Y1ZA0013), the Key Research Program of the Chinese Academy of Science (Grant KZZD-EW-13), and the National Natural Science Foundation of China (Grants 41405079 and 41105003).

## APPENDIX

### Stability Functions

The stability functions of Paulson (1970) have been implemented in the current Noah land surface model by Chen et al. (1997). Following Sun and Mahrt (1995), these stability functions are

$$\Psi_m = \begin{cases} -5\zeta, & \text{for } 0 < \zeta < 1 \\ 2 \ln[(1+x)/2] + \ln[(1+x^2)/2] - 2 \tan^{-1}(x) + \pi/2, & \text{for } -5 < \zeta < 0 \end{cases} \quad (\text{A1})$$

$$\Psi_h = \begin{cases} -5\zeta, & \text{for } 0 < \zeta < 1 \\ 2 \ln[(1+x^2)/2], & \text{for } -5 < \zeta < 0 \end{cases} \quad (\text{A2})$$

$$\zeta = z/L, \quad \text{and} \quad (\text{A3})$$

$$x = (1 - 16\zeta)^{1/4}, \quad (\text{A4})$$

where  $\Psi_m$  ( $\Psi_h$ ) is the stability correction function for momentum and (sensible heat) transfer (unitless),  $z$  is the observation height (m), and  $L$  is the Obukhov length (m).

The stability functions of Łobocki (1993) for stable conditions are (Chen et al. 1997)

$$\Psi_m = \zeta/R_{FC} - 2.076[1 - 1/(\zeta + 1)], \quad \text{for } 0 \leq \zeta < 1 \quad \text{and} \quad (\text{A5})$$

$$\Psi_h = \zeta R_{ic} / [R_{FC}^2 \varphi_T(0)] - 2.076[1 - \exp(-1.2\zeta)], \quad \text{for } 0 \leq \zeta < 1, \quad (\text{A6})$$

where  $R_{ic}$  is the critical gradient Richardson number (taken as 0.183),  $R_{FC}$  is the critical flux Richardson number (taken as 0.191), and  $\varphi_T(0)$  is the dimensionless velocity gradient for neutral conditions (taken as 0.8).

The stability function of Holtslag and De Bruin (1988) for stable conditions is

$$-\Psi_m = -\Psi_h = a\zeta + b(\zeta - cd) \exp(-d\zeta) + bc/d, \quad (\text{A7})$$

where  $a = 0.7$ ,  $b = 0.75$ ,  $c = 5$ , and  $d = 0.35$ .

## REFERENCES

- Beljaars, A. C. M., and A. A. M. Holtslag, 1991: Flux parameterization over land surfaces for atmospheric models. *J. Appl. Meteor.*, **30**, 327–341, doi:10.1175/1520-0450(1991)030<0327:FPOLSF>2.0.CO;2.
- Best, M. J., 1998: A model to predict surface temperatures. *Bound.-Layer Meteor.*, **88**, 279–306, doi:10.1023/A:1001151927113.
- Chen, F., and Y. Zhang, 2009: On the coupling strength between the land surface and the atmosphere: From viewpoint of surface exchange coefficients. *Geophys. Res. Lett.*, **36**, L10404, doi:10.1029/2009GL037980.
- , and Coauthors, 1996: Modeling of land surface evaporation by four schemes and comparison with FIFE observations. *J. Geophys. Res.*, **101**, 7251–7268, doi:10.1029/95JD02165.
- , Z. Janjić, and K. Mitchell, 1997: Impact of atmospheric surface-layer parameterizations in the new land-surface scheme of the NCEP mesoscale Eta Model. *Bound.-Layer Meteor.*, **85**, 391–421, doi:10.1023/A:1000531001463.
- Chen, X., Z. Su, Y. Ma, K. Yang, J. Wen, and Y. Zhang, 2013: An improvement of roughness height parameterization of the Surface Energy Balance System (SEBS) over the Tibetan Plateau. *J. Appl. Meteor. Climatol.*, **52**, 607–622, doi:10.1175/JAMC-D-12-056.1.
- Chen, Y., K. Yang, J. He, J. Qin, J. Shi, J. Du, and Q. He, 2011: Improving land surface temperature modeling for dry land of China. *J. Geophys. Res.*, **116**, D20104, doi:10.1029/2011JD015921.
- , —, W. Tang, J. Qin, and L. Zhao, 2012: Parameterizing soil organic carbon's impacts on soil porosity and thermal parameters for eastern Tibet grasslands. *Sci. China Earth Sci.*, **55**, 1001–1011, doi:10.1007/s11430-012-4433-0.
- Decker, M., M. A. Brunke, Z. Wang, K. Sakaguchi, X. Zeng, and M. G. Bosilovich, 2012: Evaluation of the reanalysis products from GSFC, NCEP, and ECMWF using flux tower observations. *J. Climate*, **25**, 1916–1944, doi:10.1175/JCLI-D-11-00004.1.
- de Vries, D. A., 1963: Thermal properties of soils. *Physics of Plant Environment*, W. R. van Wijk, Ed., North-Holland, 210–235.
- Dirmeyer, P. A., X. Gao, M. Zhao, Z. Guo, T. Oki, and N. Hanasaki, 2006: GSWP-2: Multimodel analysis and implications for our perception of the land surface. *Bull. Amer. Meteor. Soc.*, **87**, 1381–1397, doi:10.1175/BAMS-87-10-1381.
- Ek, M., and L. Mahrt, 1991: OSU 1-D PBL model user's guide. Oregon State University Doc., 118 pp. [Available online at

- <http://ftp.emc.ncep.noaa.gov/mmb/gcp/ldas/nceplsm/OSU1DPBL/OSU1DPBL-userguide.pdf>]
- Godfrey, C. M., and D. J. Stensrud, 2008: Soil temperature and moisture errors in operational Eta Model analyses. *J. Hydrometeorol.*, **9**, 367–387, doi:10.1175/2007JHM942.1.
- Holtzlag, A. A. M., and H. A. R. De Bruin, 1988: Applied modeling of the nighttime surface energy balance over land. *J. Appl. Meteor.*, **27**, 689–704, doi:10.1175/1520-0450(1988)027<0689:AMOTNS>2.0.CO;2.
- Jiménez, C., and Coauthors, 2011: Global intercomparison of 12 land surface heat flux estimates. *J. Geophys. Res.*, **116**, D02102, doi:10.1029/2010JD014545.
- Johansen, O., 1975: Thermal conductivity of soils. Ph.D. thesis, University of Trondheim, 236 pp.
- Kersten, M. S., 1949: Thermal properties of soils. Bull. 28, Engineering Experiment Station, University of Minnesota, 227 pp.
- Koike, T., 2004: The Coordinated Enhanced Observing Period—An initial step for integrated global water cycle observation. *WMO Bull.*, **53**, 115–121.
- , T. Yasunari, J. Wang, and T. Yao, 1999: GAME-Tibet IOP summary report. *Proc. First Int. Workshop on GAME-Tibet*, Xiafan, China, GEWEX Asian Monsoon Experiment, 1–2.
- Koster, R. D., and Coauthors, 2004: Regions of strong coupling between soil moisture and precipitation. *Science*, **305**, 1138–1140, doi:10.1126/science.1100217.
- , and Coauthors, 2006: GLACE: The Global Land–Atmosphere Coupling Experiment. Part I: Overview. *J. Hydrometeorol.*, **7**, 590–610, doi:10.1175/JHM510.1.
- Lawrence, D. M., and A. G. Slater, 2008: Incorporating organic soil into a global climate model. *Climate Dyn.*, **30**, 145–160, doi:10.1007/s00382-007-0278-1.
- Liang, X., E. F. Wood, and D. P. Lettenmaier, 1999: Modeling ground heat flux in land surface parameterization schemes. *J. Geophys. Res.*, **104**, 9581–9600, doi:10.1029/98JD02307.
- Łobocki, L., 1993: A procedure for the derivation of surface-layer bulk relationships from simplified second-order closure models. *J. Appl. Meteor.*, **32**, 126–138, doi:10.1175/1520-0450(1993)032<0126:APFTDO>2.0.CO;2.
- Ma, Y., S. Kang, L. Zhu, B. Xu, L. Tian, and T. Yao, 2008: Roof of the world—Tibetan Observation and Research Platform: Atmosphere–land interaction over a heterogeneous landscape. *Bull. Amer. Meteor. Soc.*, **89**, 1487–1492, doi:10.1175/2008BAMS2545.1.
- , and Coauthors, 2009: Recent advances on the study of atmosphere–land interaction observations on the Tibetan Plateau. *Hydrol. Earth Syst. Sci.*, **13**, 1103–1111, doi:10.5194/hess-13-1103-2009.
- Mahanama, S. P. P., R. D. Koster, R. H. Reichle, and M. J. Suarez, 2008: Impact of subsurface temperature variability on surface air temperature variability: An AGCM study. *J. Hydrometeorol.*, **9**, 804–815, doi:10.1175/2008JHM949.1.
- Mahrt, L., and M. Ek, 1984: The influence of atmospheric stability on potential evaporation. *J. Climate Appl. Meteor.*, **23**, 222–234, doi:10.1175/1520-0450(1984)023<0222:TIOASO>2.0.CO;2.
- Mölder, M., and A. Lindroth, 1999: Thermal roughness length of a boreal forest. *Agric. For. Meteorol.*, **98–99**, 659–670, doi:10.1016/S0168-1923(99)00132-X.
- Niu, G.-Y., and Coauthors, 2011: The community Noah land surface model with multiparameterization options (Noah-MP): 1. Model description and evaluation with local-scale measurements. *J. Geophys. Res.*, **116**, D12109, doi:10.1029/2010JD015139.
- Paulson, C. A., 1970: The mathematical representation of wind speed and temperature profiles in the unstable atmospheric surface layer. *J. Appl. Meteor.*, **9**, 857–861, doi:10.1175/1520-0450(1970)009<0857:TMROWS>2.0.CO;2.
- Peters-Lidard, C. D., M. S. Zion, and E. F. Wood, 1997: A soil–vegetation–atmosphere transfer scheme for modeling spatially variable water and energy balance processes. *J. Geophys. Res.*, **102**, 4303–4324, doi:10.1029/96JD02948.
- , E. Blackburn, X. Liang, and E. F. Wood, 1998: The effect of soil thermal conductivity parameterization on surface energy fluxes and temperatures. *J. Atmos. Sci.*, **55**, 1209–1224, doi:10.1175/1520-0469(1998)055<1209:TEOSTC>2.0.CO;2.
- Rosero, E., Z.-L. Yang, T. Wagener, L. E. Gulden, S. Yatheendradas, and G.-Y. Niu, 2010: Quantifying parameter sensitivity, interaction, and transferability in hydrologically enhanced versions of the Noah land surface model over transition zones during the warm season. *J. Geophys. Res.*, **115**, D03106, doi:10.1029/2009JD012035.
- Sato, T., and F. Kimura, 2007: How does the Tibetan Plateau affect the transition of Indian monsoon rainfall? *Mon. Wea. Rev.*, **135**, 2006–2015, doi:10.1175/MWR3386.1.
- Sellers, P. J., and Coauthors, 1997: Modeling the exchanges of energy, water, and carbon between continents and the atmosphere. *Science*, **275**, 502–509, doi:10.1126/science.275.5299.502.
- Seneviratne, S. I., D. Luthi, M. Litschi, and C. Schär, 2006: Land–atmosphere coupling and climate change in Europe. *Nature*, **443**, 205–209, doi:10.1038/nature05095.
- Su, Z., J. Wen, L. Dente, R. van der Velde, L. Wang, Y. Ma, K. Yang, and Z. Hu, 2011: The Tibetan Plateau observatory of plateau scale soil moisture and soil temperature (Tibet-Obs) for quantifying uncertainties in coarse resolution satellite and model products. *Hydrol. Earth Syst. Sci.*, **15**, 2303–2316, doi:10.5194/hess-15-2303-2011.
- Sun, J., and L. Mahrt, 1995: Determination of surface fluxes from the surface radiative temperature. *J. Atmos. Sci.*, **52**, 1096–1106, doi:10.1175/1520-0469(1995)052<1096:DOSFFT>2.0.CO;2.
- Taylor, K. E., 2001: Summarizing multiple aspects of model performance in a single diagram. *J. Geophys. Res.*, **106**, 7183–7192, doi:10.1029/2000JD900719.
- van der Velde, R., Z. Su, M. Ek, M. Rodell, and Y. Ma, 2009: Influence of thermodynamic soil and vegetation parameterizations on the simulation of soil temperature states and surface fluxes by the Noah LSM over a Tibetan Plateau site. *Hydrol. Earth Syst. Sci.*, **13**, 759–777, doi:10.5194/hess-13-759-2009.
- Wang, Z., X. Zeng, and M. Decker, 2010: Improving snow processes in the Noah land model. *J. Geophys. Res.*, **115**, D20108, doi:10.1029/2009JD013761.
- Wu, G., and Y. Zhang, 1998: Tibetan Plateau forcing and the timing of the monsoon onset over South Asia and the South China Sea. *Mon. Wea. Rev.*, **126**, 913–927, doi:10.1175/1520-0493(1998)126<0913:TPFATT>2.0.CO;2.
- Xia, Y., and Coauthors, 2013: Validation of Noah-simulated soil temperature in the North American Land Data Assimilation System phase 2. *J. Appl. Meteor. Climatol.*, **52**, 455–471, doi:10.1175/JAMC-D-12-033.1.
- Yang, K., T. Koike, B. Ye, and L. Bastidas, 2005: Inverse analysis of the role of soil vertical heterogeneity in controlling surface soil state and energy partition. *J. Geophys. Res.*, **110**, D08101, doi:10.1029/2004JD005500.
- , Y. Y. Chen, and J. Qin, 2009: Some practical notes on the land surface modeling in the Tibetan Plateau. *Hydrol. Earth Syst. Sci.*, **13**, 687–701, doi:10.5194/hess-13-687-2009.
- , and Coauthors, 2013: A multiscale soil moisture and freeze–thaw monitoring network on the third pole. *Bull. Amer. Meteor. Soc.*, **94**, 1907–1916, doi:10.1175/BAMS-D-12-00203.1.

- , H. Wu, J. Qin, C. Lin, W. Tang, and Y. Chen, 2014: Recent climate changes over the Tibetan Plateau and their impacts on energy and water cycle: A review. *Global Planet. Change*, **112**, 79–91, doi:[10.1016/j.gloplacha.2013.12.001](https://doi.org/10.1016/j.gloplacha.2013.12.001).
- Zeng, X., Z. Wang, and A. Wang, 2012: Surface skin temperature and the interplay between sensible and ground heat fluxes over arid regions. *J. Hydrometeor.*, **13**, 1359–1370, doi:[10.1175/JHM-D-11-0117.1](https://doi.org/10.1175/JHM-D-11-0117.1).
- Zheng, D., R. van der Velde, Z. Su, M. J. Booiij, A. Y. Hoekstra, and J. Wen, 2014: Assessment of roughness length schemes implemented within the Noah land surface model for high-altitude regions. *J. Hydrometeor.*, **15**, 921–937, doi:[10.1175/JHM-D-13-0102.1](https://doi.org/10.1175/JHM-D-13-0102.1).
- , —, —, X. Wang, J. Wen, M. J. Booiij, A. Y. Hoekstra, and Y. Chen, 2015: Augmentations to the Noah model physics for application to the Yellow River source area. Part I: Soil water flow. *J. Hydrometeor.*, **16**, 2659–2676, doi:[10.1175/JHM-D-14-0198.1](https://doi.org/10.1175/JHM-D-14-0198.1).
- Zhou, X., P. Zhao, J. Chen, L. Chen, and W. Li, 2009: Impacts of thermodynamic processes over the Tibetan Plateau on the Northern Hemispheric climate. *Sci. China*, **52D**, 1679–1693, doi:[10.1007/s11430-009-0194-9](https://doi.org/10.1007/s11430-009-0194-9).
- Zilitinkevich, S. S., 1995: Non-local turbulent transport: Pollution dispersion aspects of coherent structure of convective flows. *Air Pollution Theory and Simulation*, H. Power, N. Moussiopoulos, and C. A. Brebbia, Eds., Vol. 1, *Air Pollution III*, Computational Mechanics Publications, 53–60.